




Review Paper

# The effect of chelating agent on synthesis and electrochemical properties of $\text{LiNi}_{0.6}\text{Co}_{0.2}\text{Mn}_{0.2}\text{O}_2$

Weiwei Li<sup>1</sup>  · Lu Yao<sup>1</sup> · Xiangjun Zhang<sup>2</sup> · Wuke Lang<sup>1</sup> · Jiangju Si<sup>1</sup> · Jie Yang<sup>1</sup> · Li Li<sup>1</sup>

Received: 1 October 2019 / Accepted: 29 February 2020 / Published online: 4 March 2020

© Springer Nature Switzerland AG 2020

## Abstract

Ni-rich cathode material is one of the most promising material for Li-ion batteries (LIBs) in portable power and electric vehicles. However, how to recycle waste LIBs cathode materials is very important for environmental protection and resource utilization.  $\text{LiNi}_{0.6}\text{Co}_{0.2}\text{Mn}_{0.2}\text{O}_2$  cathode materials were prepared by sol–gel combustion method Using waste LIBs cathode materials as raw materials. The effect of different gels on the crystal structure and morphology of  $\text{LiNi}_{0.6}\text{Co}_{0.2}\text{Mn}_{0.2}\text{O}_2$  were studied by X-ray diffraction and scanning electron microscopy. The electrochemical properties were investigated by charge–discharge testing, cyclic voltammetry and electrochemical impedance spectroscopy. The results showed that the samples contained some residual C and primary crystals have been formed during combustion stage. When glucose was used as gel reagent, the sample has the good electrochemical properties with the initial discharge capacity of  $176.9 \text{ mAh g}^{-1}$ , initial coulombic efficiency of 87.0% and discharge capacity retention rate of 95.8% after 50 cycles at 0.2 C rate. The results showed that the less the cation mixing, the more complete of hexagonal crystal structure, which induced the decrease of impedance resistance and good reversibility of redox reaction.

**Keywords**  $\text{LiNi}_{0.6}\text{Co}_{0.2}\text{Mn}_{0.2}\text{O}_2$  · Sol–gel · Combustion method · Cathode material · Li-ion batteries

## 1 Introduction

Cathode materials play a key role in high-performance LIBs. Therefore, cathode materials of high power density, high safety, long cycle life and low cost for LIBs have been a research focus [1–3]. Recently,  $\text{LiNi}_{1-x-y}\text{Co}_x\text{Mn}_y\text{O}_2$  composite oxide has attracted a great deal of interest as cathode materials for LIBs due to their high specific capacity, excellent cycling performance, low cost, and good safety [4–6]. Among the compounds in the  $\text{LiNi}_{1-x-y}\text{Co}_x\text{Mn}_y\text{O}_2$  composite oxide series, nickel is mainly to improve the capacity of cathode materials, cobalt and manganese mainly to stabilize the structure of materials [7–9]. The more nickel content, the higher discharge capacity, however, it also leads to the structural instability of the

cathode materials, the serious Li/Ni ion mixing and the poor cycling performance, and so on [10–12]. In order to integrate the high capacity, long cycle life and low cost of  $\text{LiNi}_{1-x-y}\text{Co}_x\text{Mn}_y\text{O}_2$  composite oxide, many papers have focused on  $\text{LiNi}_{0.6}\text{Co}_{0.2}\text{Mn}_{0.2}\text{O}_2$  composite oxide [13–16].

At the same time, many waste LIBs have been produced. The recycling of waste LIBs is very important for environmental protection and resource utilization. The most significant aspect of waste LIBs recycling technology is how to reuse the Li, Ni, Co and Mn resource in the waste LIBs [17, 18], but re-separate different metal elements from composite metal oxides is a very complicated process.

Sol–gel method is a useful technique for preparing composite oxide due to mixing multiple metal ions uniformly at atomic or molecular scales and resulting in a

✉ Weiwei Li, lww1873851@163.com; ✉ Lu Yao, yaolu001@163.com; Xiangjun Zhang, zhangxj@glabat.com | <sup>1</sup>College of Chemistry and Chemical Engineering, Xinxiang University, Xinxiang 453003, Henan, China. <sup>2</sup>Research and Development Centre for Vehicle Battery and Energy Storage, General Research Institute for Nonferrous Metals, Beijing 100088, China.



compositionally homogeneous and nano-crystallization product. In this work, to take full use of all metal elements, fresh cathode materials were re-prepared by a simple process, using acid dissolved waste cathode materials without separation of Li, Ni, Co and Mn [19, 20].  $\text{LiNi}_{0.6}\text{Co}_{0.2}\text{Mn}_{0.2}\text{O}_2$  cathode materials were prepared by sol-gel self-combustion method, using waste LIBs cathode material as raw material, with three kinds of commonly gel reagents (citric acid, glucose and sucrose), respectively, and the effect of different gels on crystal structure and electrochemical performance of  $\text{LiNi}_{0.6}\text{Co}_{0.2}\text{Mn}_{0.2}\text{O}_2$  were researched.

## 2 Experimental

### 2.1 Preparation

Waste LIBs cathode materials we used are wasted nickel-cobalt-manganese ternary cathode materials powder, provided by a company's R&D department. The wasted nickel-cobalt-manganese ternary cathode materials powder were mixture of  $\text{LiNi}_{0.6}\text{Co}_{0.2}\text{Mn}_{0.2}\text{O}_2$ ,  $\text{LiNi}_{0.8}\text{Co}_{0.1}\text{Mn}_{0.1}\text{O}_2$  and  $\text{LiNi}_{0.5}\text{Co}_{0.2}\text{Mn}_{0.3}\text{O}_2$ , which were discards by company's R&D department. The details of the dismantle process has been reported in our preliminary work [17, 18]. The waste nickel-cobalt-manganese ternary cathode materials were dissolved in nitric acid solution under stirring with a magnetic stirrer at about 70 °C, and hydrogen peroxide was slowly added dropwise. After about 3 h, a little of insoluble material is filtered out, then, the contents of Li, Ni, Co, and Mn in the solution were determined by ICP-AES. The mole ratio of Li:Ni:Co:Mn is 1.000:0.738:0.162:0.322. Afterward, the desired metal element ( $\text{Li}_2\text{CO}_3$ ,  $\text{Ni}(\text{NO}_3)_2$ ,  $\text{Mn}(\text{NO}_3)_2$  and  $\text{Co}(\text{NO}_3)_2$ ) was added to the solution in order to make the stoichiometric ratio of Li:Ni:Co:Mn equal to 1.05:0.6:0.2:0.2 (molar ratio). Excess lithium was added to compensate for lithium ion loss, which occurs at high temperature. Measured 100 ml of the solution in a beaker, then placed in a water bath at 80 °C. And next, adding a certain amount of gel agent (citric acid, glucose or sucrose) in the beaker under stirring with a magnetic stirrer until a viscous gel was obtained. The molar ratio of citric acid to metal ions was 2:1. Ammonia was added in the mixed solution until pH value was about 6.0. The resulting viscous gel was dried in a vacuum oven at 120 °C for 12 h, subsequently the dry gel was placed in a crucible and ignited with open fire to remove nitrate and gel, avoiding volume expansion during calcination.

Finally, the self-propagating combustion samples were calcined at 500 °C and 850 °C for 2 h and 12 h under an air atmosphere with a flow rate of about 50 mL/min, respectively. When citric acid, glucose, or sucrose was used as gel

agent, the corresponding resultant sample was designated as C-622, G-622 and S-622, respectively.

### 2.2 Characterization

The content of the elements was determined by PE Optima8300 Jegger Coupling Plasma Optical Emission Spectrograph (ICP-AES). The thermogravimetry and differential scanning calorimetry (TG-DSC) was analyzed by a German Netzsch STA449 F3 simultaneous thermal analyzer, the temperature range was from room temperature to 900 °C, and the heating rate was 10 °C/min. The morphology was observed with an American FEI Quanta Feg 250 scanning electron microscope (SEM) operating at 10 kV. The specific surface area of the material was measured by the automatic specific surface and pore size distribution analyzer (NOVA 2200E) of Conta Company, USA. The structural information of synthesized samples was characterized by a German Bruker X-Ray diffraction (XRD) (Rigaku  $\theta/\theta$  diffractometer with  $\text{CuK}\alpha$  radiation ( $r = 1.54056 \text{ \AA}$ )), the scanning rate was 10°/min, and the scanning range of the diffraction angle ( $2\theta$ ) was  $15^\circ \leq 2\theta \leq 70^\circ$ .

### 2.3 Electrochemical measurement

The electrochemical properties were measured using a CR2016 coin-type half-cell, which contains a cathode and a Li metal anode separated by a porous polypropylene film. The cathode slurry was prepared by homogeneously mixing the active material, acetylene black and polypropylene difluoride binder in a mass ratio of 8:1:1 in N-methyl-2-pyrrolidone (NMP) solvent. Then the slurry was uniform coating onto an aluminum foil. After drying, electrode laminate was punched into disks (14 mm in diameter) and dried in a vacuum oven at 105 °C overnight. The cells were assembled in an Argon-filled glove box. The electrolyte was 1 mol L<sup>-1</sup>  $\text{LiPF}_6$  dissolved in ethylene carbonate (EC) and dimethyl carbonate (DMC) (1:1 in volume). In the CR2016 coin-type half-cell, the quality of the active electrode material is 0.0150–0.0200 mg, and the electrolyte added to the coin cell was amount 2–3 drops.

The charge/discharge tests were examined on a China Neware cell test system controlled by computer, cells were set to be discharged and charged between 2.75 and 4.25 V at 0.2 C (1 C = 250 mAh g<sup>-1</sup>). Cyclic voltammograms (CV) measurements were done by a Holand Ivium electrochemical workstation between 2.75 and 4.5 V at a scan rate of 0.1 mV/s. Electrochemical impedance spectroscopies (EIS) were performed on constant potential (3.6 V) at room temperature. The frequency range was 0.01 Hz–100 kHz at alternating current (AC) signal amplitude of 10 mV.

### 3 Results and discussion

#### 3.1 Thermal analysis of the self-propagating combustion products

Thermogravimetry and differential scanning calorimetry (TG-DSC) curves of the self-propagating combustion samples of three different gels were showed in Fig. 1. and the corresponding self-propagating combustion sample was designated as BHC-622, BHG-622 and BHS-622, respectively when citric acid, glucose, and sucrose was gel reagents.

It can be seen from Fig. 1a, the weight loss trends of the three samples are very similar, which can be divided into three stages. In the first stage, all the three samples weight loss was about 4.9% before 265.5 °C, which can be attributed to the dehydration of absorbed water. In the second stage, the weight loss of BHC-622, BHG-622 and BHS-622 were about 24.2%, 14.8% and 20.9%, respectively, which was mainly attributed to the decomposition of the dried gels. The weight loss of BHC-622, BHG-622 and BHS-622 in the third stage was 5.1%, 7.2% and 5.1%, respectively, can be attributed to the oxygen loss of composite oxides. The weight loss of BHG-622 is the most among the three samples may be due

to BHG-622 still has a small amount of residual C after 448.7 °C, which may lead to smaller particles during calcination.

The DSC curves of BHC-622, BHG-622 and BHS-622 are also very similar, which can be observed in Fig. 1b. The first sharp exothermic peak corresponds to the decomposition of the dried gels. the peak temperature of BHC-622, BHG-622 and BHS-622 is 443.7 °C, 411.3 °C and 401.8 °C, respectively. The weak and wide exothermic peaks after 500 °C of the three samples may be caused by oxygen loss and change into regular layered crystals of the composite oxides the minimum and maximum central temperature of exothermic peak is BHC-622 and BHS-622, respectively. The minimum releasing heat and peak temperature of BHC-622 may be due to the maximum releasing heat during the self-propagating combustion process of BHC-622 among the three samples, which because of self-propagating combustible of BHC-622 is not only citric acid, but also ammonium nitrate, resulting in relatively best crystalline sample is formed preliminary and minimum energy is required for subsequently crystallization among the three products.

The morphology of C-622, G-622 and S-622 are shown in Fig. 2a–c. Three of the samples are consist of irregular agglomeration by uniformly primary particle. The average primary particle sizes of C-622, G-622 and S-622 is about 0.705 μm, 0.701 μm and 0.872 μm by calculated 20 random

**Fig. 1** Thermal analysis curves of the self propagating combustion samples of three different gels

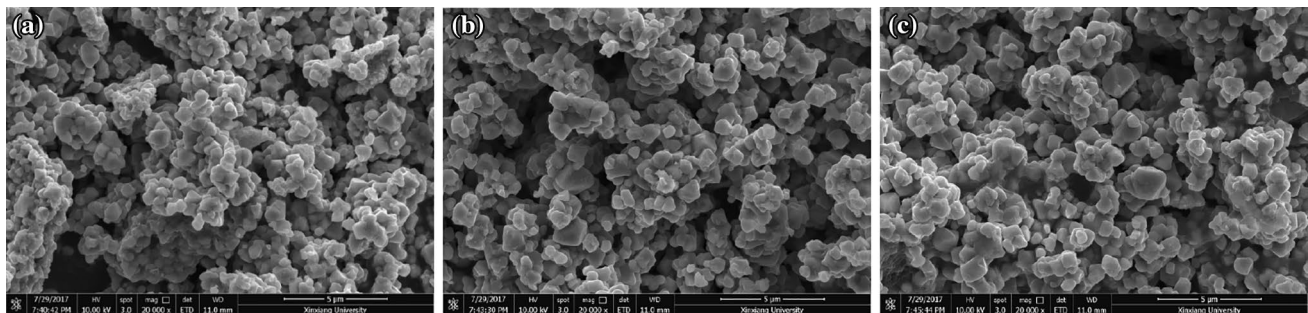
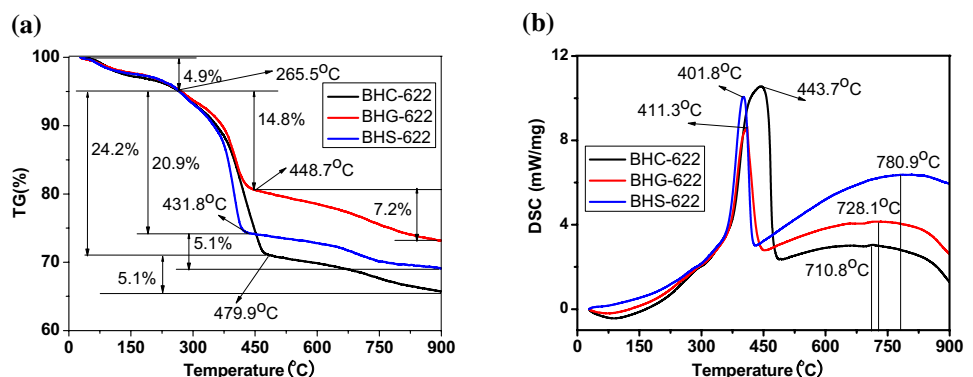


**Fig. 2** The SEM images of **a** C-622, **b** G-622, and **c** S-622

particles with a ruler, respectively. The average primary particle size of S-622 is the largest, C-622 and G-622 are almost same. It is generally believed that when the primary particle size is small, the active particles can be sufficiently infiltrated by the electrolyte, which is favorable for electrochemical performance via enhanced insertion/discharge of  $\text{Li}^+$  [21, 22].

In order to study the agglomeration of primary particles, the specific surface area of three samples were measured by automatic surface area and pore size distribution analyzer. The specific surface areas of C-622, G-622 and S-622 are about  $5.71 \text{ m}^2/\text{g}$ ,  $5.42 \text{ m}^2/\text{g}$  and  $4.59 \text{ m}^2/\text{g}$ , respectively. So, the agglomeration degree of primary particles of C-622 and G-622 is lesser and almost the same, but that of S-622 is more serious, which correspond to the average particle size of C-622, G-622 and S-622.

The primary particle size of C-622 is uniform and smaller, because of the more pores impeded the contact between primary particles in the calcination process, which is owing to more residual C after the self-propagating combustion. Although the G-622 has less residual C after the self-propagating combustion, and the residual C still exists after  $448.7^\circ\text{C}$ , which also hinder the contact between the primary particles in the calcination process, resulting in the primary particle size of C-622 more uniform and smaller. However, the average primary particle size of the S-622 is relatively larger than that of C-622 and G-622 may be due to space hindrance effect is less than that of C-622 and G-622, which because of residual C of S-622 is less than C-622 after self-propagating combustion and no residual C after  $431.8^\circ\text{C}$ .

Figure 3 displays the XRD patterns of BHC-622, BHG-622 and BHS-622. As can be seen from the patterns that the crystal structure of the three samples have been preliminaries formed. Comparing the strength of the peak (003) and the value of  $I_{003}/I_{104}$ , the highest and the lowest

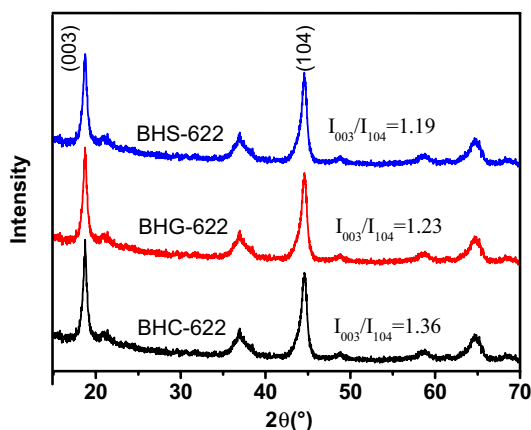


**Fig. 3** The XRD patterns of the self propagating combustion products

is BHC-622 and BHS-622, respectively, indicating that the best crystalline is BHC-622 which formed during the self-propagating combustion process, may be owing to the maximum releasing heat by BHC-622 during the self-propagating combustion process, however, BHS-622 is just the opposite. The diffraction peaks such as (101), (006) (102) and (108) (110) are not separated, indicating that the three samples need further heat treatment to form a good layered structure.

Figure 4 shows the XRD patterns of C-622, G-622 and S-622. All the XRD patterns exhibited well defined layer structure based on a hexagonal  $\alpha\text{-NaFeO}_2$  structure with a R-3 m space group [23, 24]. No diffraction peaks of any impurities are detected, and the baseline of each pattern is at the same level, indicating that the residual C has been completely removed after high temperature calcination. The distinct splitting of (006)/(102) and (108)/(110) peaks indicates a well-developed layered structure in the three samples [25, 26]. The  $I_{003}/I_{104}$  value of C-622, G-622 and S-622 is 1.53, 1.70 and 1.59, respectively, indicating that the cation mixing of G-622 is the smallest among the three samples [27, 28].

The lattice parameters were obtained via refining and calculating in Bruker DIFFRAC EVA software, as showed in Table 1. The value of  $c/a$  reflects the trigonometric distortion of the main structure, and the higher the value, the more complete of layered hexagonal structure [29, 30]. It can be observed in the Table 1 that the G-622 has a most

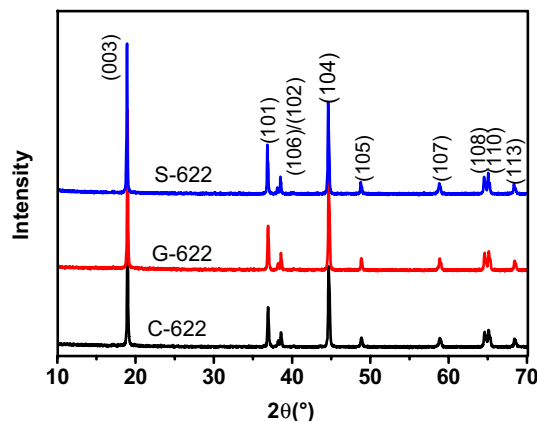


**Fig. 4** The X-ray diffraction patterns of C-622, G-622 and S-622

**Table 1** The lattice parameters of C-622, G-622 and S-622

| Samples | a/nm   | c/nm   | c/a    |
|---------|--------|--------|--------|
| C-622   | 0.2878 | 1.4191 | 4.9308 |
| G-622   | 0.2856 | 1.4266 | 4.9951 |
| S-622   | 0.2849 | 1.4151 | 4.9670 |

ordered  $\alpha$ - $\text{NaFeO}_2$  structure among the three samples, which indicate that it has the best structural stability.

From the analysis of Figs. 1, 3 and 4, it can be known that the preliminaries formed crystalline of BHC-622 is the strongest and the temperature of reheat treatment of BHC-622 is the lowest after self-propagating combustion, however, the cation mixing and the hexagonal layered structure of C-622 are highest and worst, may be caused by higher temperature or longer time of heat treatment. Meanwhile, the preliminaries formed crystalline of BHS-622 is the weakest and the temperature of reheat treatment of BHS-622 is the highest, but the cation mixing and the layered hexagonal structure of S-622 are higher and worse than G-622, may be caused by lower temperature or shorter time of heat treatment.

Figure 5 displays the initial charge/discharge curves (a) and cycling performance curves (b) of C-622, G-622 and S-622 between 2.75 and 4.25 V at 0.2 C at room temperature. According to Fig. 5a, the initial discharge capacity of C-622, G-622 and S-622 are  $168.6 \text{ mAh g}^{-1}$ ,  $176.9 \text{ mAh g}^{-1}$  and  $182.8 \text{ mAh g}^{-1}$ , and initial coulombic efficiency of C-622, G-622 and S-622 are 82.5%, 87.0% and 85.9%, respectively. Capacity retention of C-622, G-622 and S-622 after 50 cycles were counted according to Fig. 5b, which is 86.3%, 95.8% and 89.3%, respectively. Although the initial discharge capacity of S-622 is higher than that of G-622, but initial coulombic efficiency and the discharge capacity after 50 cycles of S-622 is lower than that of G-622.

The cells were charge/discharge at 0.2 C, 1.0 C, 2.0 C and 0.2 C for every 10 cycles between 2.75 and 4.25 V at room temperature, respectively, the rate capabilities of the three samples were shown in Fig. 6. The discharge capacity is reduced as the growth of current density because of the growing polarization. Apparently, G-622 electrode shows a better rate capability than the other two, implying that it has great potential to be used as power battery. The results

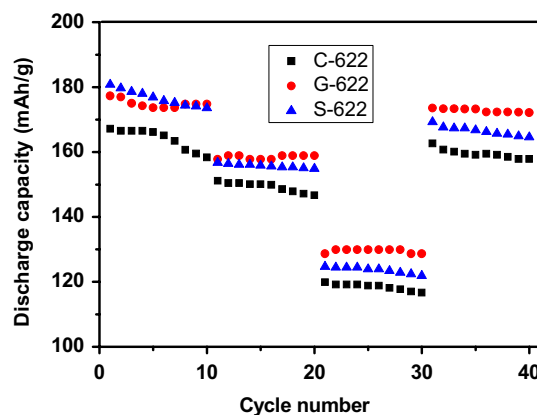


Fig. 6 The rate capability of C-622, G-622 and S-622

indicate that the electrochemical performance of G-622 is the best, which is due to the lowest cation mixing in G-622 and the highest structural integrity of the layered hexagonal structure.

The average primary particle sizes and agglomeration of C-622 are less than S-622, the structural stability of S-622 is better than C-622, but the electrochemical performance of S-622 is better than C-622, according to the analysis of morphology, structure and electrical performance, which possible to conclude that the effect of the structure is greater than the effect of the morphology on the electrochemical performance of the materials.

Figure 7 displays the EIS results of the three electrodes after 50 cycles at 0.2 C, which can be studied the magnitude of the impedance of  $\text{Li}^+$  during insertion and extraction [31, 32]. The intercept of the Z axis corresponds to the ohmic resistance ( $R_s$ ) of electrolyte between the working electrode and the reference electrode, the semicircle in the high frequency range is associated with cathode interface film resistance ( $R_{SEI}$ ), the second semicircle in the middle

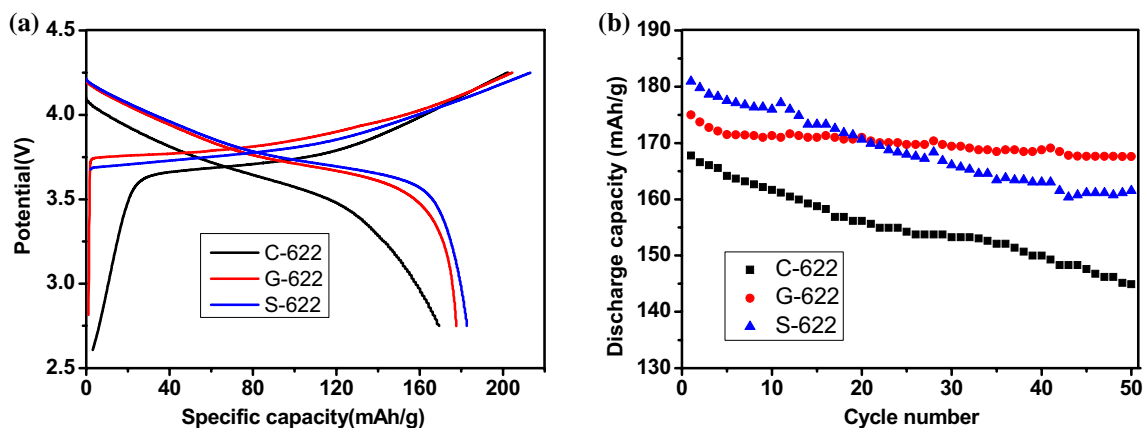


Fig. 5 The initial charge/discharge (a) and 50 cycles discharge (b) curves of C-622, G-622 and S-622

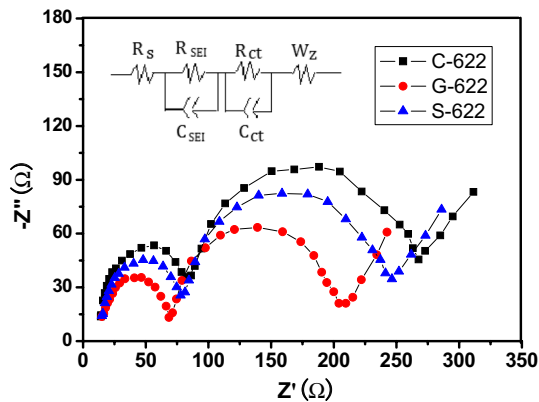


Fig. 7 The EIS curves of C-622, G-622 and S-622

frequency is assigned to the charge transfer resistance ( $R_{ct}$ ), and a oblique straight line in the low frequency is assigned to the  $\text{Li}^+$  diffusion coefficient  $W_z$ , the smaller the slope, the greater the impedance [33–37].

The impedance parameters simulated using the equivalent circuit are listed in Table 2, which were simulated by Zview software, it can be clearly seen that the minimum and maximum of resistance is G-622 and C-622, respectively, which can be determinate by the structural stability of C-622 is worst, the initial particle size of S-622 is largest, the structural stability of G-622 is best, among the three electrodes.

Figure 8 shows the CV results of three electrodes between 2.75 and 4.5 V with a scanning rate of  $0.1 \text{ mV s}^{-1}$  after 50 cycles. A pair of anodic and cathodic peaks in the scan is observed which associated with the oxidation/reduction reactions of  $\text{Ni}^{2+} \leftrightarrow \text{Ni}^{4+}$ , indicating that the reversibility of  $\text{Li}^+$  intercalation and deintercalation in the layered crystal structure [38–41].

As showing in Fig. 8, intensities of anodic and cathodic peaks of G-622 electrode are strongest among the three electrodes, the potential difference ( $\Delta E_p$ ) between the oxidation and reduction peaks for the C-622, G-622 and S-622 electrode are 0.178 V, 0.084 V and 0.121 V, respectively, which illustrates G-622 has a relatively lowest polarization and best electrochemical reversibility, indicating that it has the best structural stability in the process of charging and discharging.

**Table 2** The impedance parameters of C-622, G-622 and S-622

| Samples | $R_s$ ( $\Omega$ ) | $R_{SEI}$ ( $\Omega$ ) | $R_{ct}$ ( $\Omega$ ) | Sum ( $\Omega$ ) |
|---------|--------------------|------------------------|-----------------------|------------------|
| C-622   | 14.13              | 84.26                  | 267.47                | 365.86           |
| G-622   | 15.12              | 68.37                  | 207.15                | 290.64           |
| S-622   | 15.04              | 78.69                  | 246.83                | 340.56           |

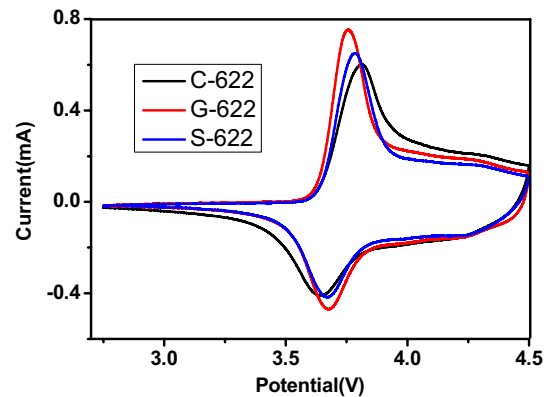


Fig. 8 The CV curve of samples after 50 weeks cycle at room temperature ( $0.1 \text{ mV s}^{-1}$ )

## 4 Conclusions

Layered  $\text{LiNi}_{0.6}\text{Co}_{0.2}\text{Mn}_{0.2}\text{O}_2$  cathodes was prepared by sol–gel self propagating combustion method using waste Lithium-ion batteries (LIBs) cathode materials as raw materials, and the effect of different gel was investigated. The sample after self-propagating combustion still contains much residual C, the most and least residual C are BHC-622 and BHG-622. The primary crystals have been formed after self-propagating combustion, the best and worst are BHC-622 and BHS-622, but need further heat treatment to form a good layered structure. The average primary particle size of S-622 is largest, nevertheless C-622 and G-622 are nearly the same. The structure influence on electrochemical performance is greater than morphology. The best electrochemical performance with initial discharge capacity is  $176.9 \text{ mAh g}^{-1}$ , initial coulombic efficiency is 87.0% and discharge capacity retention rate is 95.8% after 50 cycles at 0.2 C rate is obtained, when glucose used as gel, which due to least cation mixing, most complete hexagonal crystal structure, least impedance and best reversibility of redox reaction. We believe that the very meaningful work is very important to reuse waste LIBs cathode materials and its impacts on the electrochemical performances of the cathode materials will open a new way to synthesis the cathode materials.

**Acknowledgements** This study was partially supported by the National Natural Science Foundation of China (Nos. 51901201 and No.51701173) and Key Scientific Research Project of Colleges and Universities in Henan Province (Nos.19A610008 and 20B430015).

## Compliance with ethical standards

**Conflict of interest** The author(s) declare that they have no competing interests.

## References

- Zhai YW, Zhang JC, Zhao H, Hu ZB, Liu XF (2017) Research progress of ternary layered oxide cathode materials for lithium ion batteries. *J Eng Stud* 9:523–537
- Gao WC, Pan FF, Xiang DB, Li YX (2018) Research progress of  $\text{LiMnPO}_4$  cathode material for Li-ion batteries. *Chin J Power Sources* 42:445–447
- Qin JX, Jiang Q, Li H, Liu QQ, Duan ZH, Lu XY (2018) Research progress of the structural optimization design and electrochemical performances on the Li-rich manganese-based cathode materials. *J Funct Mater* 28:3007–3012
- Liang CP, Kong FT, Longo RC, Zhang CX, Nie YF, Zheng YP, Cho K (2017) Site-dependent multicomponent doping strategy for Ni-rich  $\text{LiNi}_{1-2y}\text{Co}_y\text{Mn}_y\text{O}_2$  ( $y = 1/12$ ) cathode materials for Li-ion batteries. *J Mater Chem A* 48:25303–25313
- Chen Z, Chao DL, Lin JY (2017) Recent progress in surface coating of layered  $\text{LiNi}_x\text{Co}_y\text{Mn}_z\text{O}_2$  for lithium-ion batteries. *Mater Res Bull* 96:491–502
- Liu W, Li XF, Xiong DB (2018) Significantly improving cycling performance of cathodes in lithium ion batteries: the effect of  $\text{Al}_2\text{O}_3$  and  $\text{LiAlO}_2$  coatings on  $\text{LiNi}_{0.6}\text{Co}_{0.2}\text{Mn}_{0.2}\text{O}_2$ . *Nano Energy* 44:111–120
- Myung ST, Maglia F, Park KJ, Yoon CS, Lamp P, Kim SJ, Sun YK (2017) Nickel-rich layered cathode materials for automotive lithium-ion batteries: achievements and perspectives. *ACS Energy Lett* 2:196–223
- Park K, Park JH, Choi B, Kim JH, Hong SG, Han HN (2017) Metal phosphate-coated Ni-rich layered oxide positive electrode materials for Li-ion batteries: improved electrochemical performance and decreased Li residuals content. *Electrochim Acta* 257:217–223
- Kaneda H, Koshika Y, Nakamura T (2017) Improving the Cycling performance and thermal stability of  $\text{LiNi}_{0.6}\text{Co}_{0.2}\text{Mn}_{0.2}\text{O}_2$  cathode materials by Nb-doping and surface modification. *Int J Electrochem Sci* 12:4640–4653
- Liang C, Kong F, Longo RC, Kc S, Kim JS, Jeon S, Choi S, Cho K (2016) Unraveling the origin of instability in Ni-rich  $\text{LiNi}_{1-2x}\text{Co}_x\text{Mn}_x\text{O}_2$  (NCM) cathode materials. *J Phys Chem C* 120:6383–6393
- Li X, Ge WJ, Wang H, Qu MZ (2017) Research progress on the capacity fading mechanisms of high-nickel ternary layered oxide cathode materials. *J Inorg Mater* 32:113–121
- Liu W, Oh P, Liu XE (2015) Nickel-Rich layered lithium transition-metal oxide for high-energy lithium-ion batteries. *Angew Chem Int Ed* 54:4440–4457
- Liu SY, Chen X, Zhao JY (2018) Uncovering the role of Nb modification in improving the structure stability and electrochemical performance of  $\text{LiNi}_{0.6}\text{Co}_{0.2}\text{Mn}_{0.2}\text{O}_2$  cathode charged at higher voltage of 4.5 V. *J Power Sources* 374:149–157
- Xue LL, Li YJ, Xu B, Chen YX, Cao GL, Li JG, Deng SY, Chen YJ, Chen J (2018) Effect of Mo doping on the structure and electrochemical performances of  $\text{LiNi}_{0.6}\text{Co}_{0.2}\text{Mn}_{0.2}\text{O}_2$  cathode material at high cut-off voltage. *J Alloy Compd* 748:561–568
- Fu JL, Mu DB, Wu BR, Bi JY, Cui H, Yang H, Wu HF, Wu F (2018) Electrochemical properties of the  $\text{LiNi}_{0.6}\text{Co}_{0.2}\text{Mn}_{0.2}\text{O}_2$  cathode material modified by lithium tungstate under high voltage. *ACS Appl Mater Interfaces* 10:19704–19711
- Liao B, Hu XL, Xu MQ, Li HY, Yu L, Fan WZ, Xing LD, Liao YH, Li WS (2018) Constructing unique cathode interface by manipulating functional groups of electrolyte additive for graphite/ $\text{LiNi}_{0.6}\text{Co}_{0.2}\text{Mn}_{0.2}\text{O}_2$  cells at high voltage. *J Phys Chem Lett* 9:3434–3445
- Yao L, Feng Y, Xi GX (2015) A new method for the synthesis of  $\text{LiNi}_{1/3}\text{Co}_{1/3}\text{Mn}_{1/3}\text{O}_2$  from waste lithium ion batteries. *RSC Adv* 5:44107–44114
- Yao L, Yao HS, Xi GX, Feng Y (2016) Recycling and synthesis of  $\text{LiNi}_{1/3}\text{Co}_{1/3}\text{Mn}_{1/3}\text{O}_2$  from waste lithium ion batteries using D,L-malic acid. *RSC Adv* 6:17947–17954
- Lee SW, Kim MS, Jeong JH (2017)  $\text{Li}_3\text{PO}_4$  surface coating on Ni-rich  $\text{LiNi}_{0.6}\text{Co}_{0.2}\text{Mn}_{0.2}\text{O}_2$  by a citric acid assisted sol-gel method: improved thermal stability and high-voltage performance. *J Power Sources* 360:206–214
- Zhang YJ, Hao T, Huang XS, Duan JG, Meng Q, Wang D, Lin Y, Xu ML, Dong P (2019) Synthesis of high performance nano-overlithiated oxide coated  $\text{LiNi}_{0.6}\text{Co}_{0.2}\text{Mn}_{0.2}\text{O}_2$  from spent lithium ion batteries. *Mater Res Express* 8:085521
- Lee SW, Kim HG, Kim MS, Youn HC, Kang K, Cho BW, Roh KC, Kim KB (2016) Improved electrochemical performance of  $\text{LiNi}_{0.6}\text{Co}_{0.2}\text{Mn}_{0.2}\text{O}_2$  cathode material synthesized by citric acid assisted sol-gel method for lithium ion batteries. *J Power Sources* 315:261–268
- Wang Q, Shen CH, Shen SY, Xu YF, Shi CG, Huang L, Li JT, Sun SG (2017) Origin of structural evolution in capacity degradation for overcharged NMC622 via operando coupled investigation. *ACS Appl Mater Interfaces* 9:24731–24742
- Liu L, Li JF, Bao SS, He H, Li YJ, Sun WX, Yue B, Huang Y, Zhang PC (2019) Electrochemical properties of  $\text{LiNi}_{0.6}\text{Co}_{0.12}\text{Mn}_{0.2}\text{V}_{0.08}\text{O}_2$  as the tetrad cathode material of lithium-ion battery under high cut-off voltages. *J Solid State Electrochem* 23:2009–2019
- Du K, Xie HB, Hu GR, Peng ZD, Cao YB, Yu F (2016) Enhancing the thermal and upper voltage performance of Ni-rich cathode material by a homogeneous and facile coating method: spray-drying coating with nano- $\text{Al}_2\text{O}_3$ . *ACS Appl Mater Interfaces* 27:17713–17720
- Liu S, Chen X, Zhao J, Su J, Zhang C, Huang T, Wu J, Yu A (2018) Uncovering the role of Nb modification in improving the structure stability and electrochemical performance of  $\text{LiNi}_{0.6}\text{Co}_{0.2}\text{Mn}_{0.2}\text{O}_2$  cathode charged at higher voltage of 4.5 V. *J Power Sources* 374:149–157
- Kong JZ, CheY CYQ, Wang QZ, Li AD, Li H, Zhou F (2019) Enhanced electrochemical performance of Ni-rich  $\text{LiNi}_{(0.6)}\text{Co}_{(0.2)}\text{Mn}_{(0.2)}\text{O}_{(2)}$  coated by molecular layer deposition derived dual-functional C- $\text{Al}_2\text{O}_3$  composite coating. *J Alloys Compd* 799:89–98
- Cho WS, Kim SM, Lee KW (2016) Investigation of new manganese orthophosphate  $\text{Mn}_3(\text{PO}_4)_2$  coating for nickel-rich  $\text{LiNi}_{0.6}\text{Co}_{0.2}\text{Mn}_{0.2}\text{O}_2$  cathode and improvement of its thermal properties. *Electrochim Acta* 198:77–83
- Fu JL, Mu DB, Wu BR, Bi JY, Liu XJ, Peng YY, Li YQ, Wu F (2017) Enhanced electrochemical performance of  $\text{LiNi}_{0.6}\text{Co}_{0.2}\text{Mn}_{0.2}\text{O}_2$  cathode at high cutoff voltage by modifying electrode/electrolyte interface with lithium metasilicate. *Electrochim Acta* 246:27–34
- Zhao ZK, Chen S, Mu DB, Ma R, Li CL, Wu BR, Wu F, Cheng KL, Xie CX (2019) Understanding the surface decoration on primary particles of nickel-rich layered  $\text{LiNi}_{0.6}\text{Co}_{0.2}\text{Mn}_{0.2}\text{O}_2$  cathode material with lithium phosphate. *J Power Sources* 431:84–92
- Wang Q, Shen CH, Shen SY (2017) Origin of structural evolution in capacity degradation for overcharged NMC622 via operando coupled investigation. *ACS Appl Mater Interfaces* 9:24731–24742
- Du K, Huang J, Cao Y, Peng Z, Hu G (2013) Study of effects on  $\text{LiNi}_{0.8}\text{Co}_{0.15}\text{Al}_{0.05}\text{O}_2$  cathode by  $\text{LiNi}_{1/3}\text{Co}_{1/3}\text{Mn}_{1/3}\text{O}_2$  coating for lithium ion batteries. *J Alloys Compd* 574:377–382
- Chen T, Li X, Wang H, Yan XX, Wang L, Deng BW, Ge WJ, Qu MZ (2018) The effect of gradient boracic polyanion-doping on structure, morphology, and cycling performance of Ni-rich  $\text{LiNi}_{0.8}\text{Co}_{0.15}\text{Al}_{0.05}\text{O}_2$  cathode material. *J Power Sources* 374:1–11

33. Liang CH, Liu LB, Jia Z, Dai C, Xiong Y (2015) Synergy of nyquist and bode electrochemical impedance spectroscopy studies to particle size effect on the electrochemical properties of  $\text{LiNi}_{0.5}\text{Co}_{0.2}\text{Mn}_{0.3}\text{O}_2$ . *Electrochim Acta* 186:413–419
34. Wang M, Zhang R, Gong YQ, Su YF, Xiang DB, Chen L, Chen YB, Luo M, Chu M (2017) Improved electrochemical performance of the  $\text{LiNi}_{0.8}\text{Co}_{0.1}\text{Mn}_{0.1}\text{O}_2$  material with lithium-ion conductor coating for lithium-ion batteries. *Solid State Ion* 312:53–60
35. Chen YX, Tang SY, Deng SY, Lei TX, Li YJ, Li W, Cao GL, Zhu J, Zhang JP (2019) Chemical coupling constructs amorphous silica modified  $\text{LiNi}_{0.6}\text{Co}_{0.2}\text{Mn}_{0.2}\text{O}_2$  cathode materials and its electrochemical performances. *J Power Sources* 431:8–16
36. Li YJ, Chen YX, Luo LS, Ming XQ, Li JG, Lei TX, Deng SY, Guo J, Zhu J, Chang SH (2019) Surface in-situ reconstruction of  $\text{LiNi}_{0.8}\text{Co}_{0.1}\text{Mn}_{0.1}\text{O}_2$  cathode materials interacting with antimony compounds and the electrochemical performances. *J Electroanal Chem* 854:113582
37. Chen YX, Li YJ, Li W, Cao GL, Tang SY, Su QY, Deng SY, Guo J (2018) High-voltage electrochemical performance of  $\text{LiNi}_{0.5}\text{Co}_{0.2}\text{Mn}_{0.3}\text{O}_2$  cathode material via the synergetic modification of the Zr/Ti elements. *Electrochim Acta* 281:48–59
38. Zhang XD, Shi JL, Liang JY, Wang LP, Yin YX, Jiang KC, Guo YG (2019) An effective  $\text{LiBO}_2$  coating to ameliorate the cathode/electrolyte interfacial issues of  $\text{LiNi}_{0.6}\text{Co}_{0.2}\text{Mn}_{0.2}\text{O}_2$  in solid-state Li batteries. *J Power Sources* 426:242–249
39. Sun S, Du C, Qu D, Zhang X, Tang Z (2015)  $\text{Li}_2\text{ZrO}_3$ -coated  $\text{LiNi}_{0.6}\text{Co}_{0.2}\text{Mn}_{0.2}\text{O}_2$  for high-performance cathode material in lithium-ion battery. *Ionics* 21:2091–2100
40. Hu GR, Qi XY, Hu KH, Lai XW, Zhang X, Du K, Peng ZD, Cao YB (2018) A facile cathode design with a  $\text{LiNi}_{0.6}\text{Co}_{0.2}\text{Mn}_{0.2}\text{O}_2$  core and an  $\text{AlF}_3$ -activated  $\text{Li}_{1.2}\text{Ni}_{0.2}\text{Mn}_{0.6}\text{O}_2$  shell for Li-ion batteries. *Electrochim Acta* 265:391–399
41. Chen YX, Li YJ, Tang SY, Lei TX, Deng SY, Xue LL, Cao GL, Zhu J (2018) Enhanced electrochemical properties of the Cd-modified  $\text{LiNi}_{0.6}\text{Co}_{0.2}\text{Mn}_{0.2}\text{O}_2$  cathode materials at high cut-off voltage. *J Power Sources* 395:403–413

**Publisher's Note** Springer Nature remains neutral with regard to jurisdictional claims in published maps and institutional affiliations.